Microchimica Acta (2026) 193:386
https://doi.org/10.1007/s00604-026-08107-2

RESEARCH

A ratiometric luminescent nanoprobe based on Eu^{3+}-modified zinc gallogermanate for smartphone-assisted visual detection of tetracycline in food samples

Xue-Yang Huang[1,2] · Li-Xia Yan[3] · Xu Zhao[1,2] · Hua Lin[4] · Li-Jian Chen[1,2] · Xiu-Ping Yan[1,2]

Received: 13 March 2026 / Accepted: 1 May 2026

Abstract

Residual tetracycline-class antibiotics (TCs) in animal-derived foods pose significant risks to human health, underscoring the demand for simple, low-cost, and on-site detection techniques. Herein, a ratiometric luminescent nanoprobe was developed based on Eu^{3+}-modified zinc gallogermanate (ZGGO) nanoparticles. The addition of tetracycline (TC) enhanced the Eu^{3+} emission at 618 nm via the antenna effect, while the intrinsic emission of ZGGO at 465 nm was quenched through an inner filter effect. This dual-response enabled the quantitative detection of TC. The luminescence intensity ratio (I_{618}/I_{465}) showed excellent linearity with TC concentration in the range 0.2–70 μmol L^{-1} ($R^2 = 0.9912$), with a detection limit of 169.5 nmol L^{-1}. Moreover, a smartphone-assisted portable platform was constructed for visual on-site analysis. The R/B value correlated linearly with TC concentrations (0.1 to 55 μmol L^{-1}, $R^2 = 0.9968$), achieving a detection limit of 85.9 nmol L^{-1}. The spiked recoveries measured by both methods in three fish samples ranged from 86.1% to 117.8%, and the results were reliably verified by the traditional high-performance liquid chromatography method, demonstrating the potential of the bimodal strategy for rapid screening of TCs in complex matrix samples.

Keywords Zinc gallogermanate · Ratiometric luminescent probe · Visual detection · Smartphone-assisted color detection · Tetracycline residues

Introduction

Tetracycline-class antibiotics (TCs) are broad-spectrum agents effective against a wide range of Gram-positive and Gram-negative bacteria [1, 2]. Owing to their advantageous properties, including low cost, high antibacterial efficacy, good oral bioavailability, and minimal toxicity [3, 4], TCs are extensively utilized in animal husbandry and aquaculture. However, the overuse of TCs in agriculture can lead to the accumulation of tetracycline (TC) residues in various food products, including milk, eggs, fish, and meat [5], thereby raising concerns about concerns over chronic dietary exposure, which is associated with potential health risks ranging from tooth discoloration and allergic reactions to more severe conditions such as gastrointestinal disturbances and liver damage [6]. In response, the U.S. Food and Drug Administration has established a tolerance level of 2 mg L^{-1} (approximately 4.5 μmol L^{-1}) for TC residues in poultry muscle. Therefore, developing methods for the rapid and accurate monitoring of tetracycline levels in food products is of paramount importance.

Currently, the detection of TCs primarily relies on well-established techniques such as high-performance liquid chromatography (HPLC) [7], gas chromatography [8], mass spectrometry [9], and liquid chromatography-mass spectrometry method [10]. However, these methods generally require extensive sample preparation, sophisticated instrumentation, and trained operators, thereby restricting their use predominantly to centralized laboratories.

✉ Li-Jian Chen
chenlijian123@jiangnan.edu.cn

1 Institute of Analytical Food Safety, School of Food Science and Technology, Jiangnan University, Wuxi 214122, China

2 Key Laboratory of Screening, Prevention, and Control of Food Safety Risks, State Administration for Market Regulation, Wuxi 214122, China

3 Analysis and Testing Center, Jiangnan University, Wuxi 214122, China

4 Food Safety Detection Key Laboratory of Sichuan Province, Chengdu 610041, China

Published online: 12 May 2026

Consequently, the development of sensitive, cost-effective, and user-friendly sensors is imperative for the rapid detection of TCs and to address these inherent limitations.

Fluorescence sensing is increasingly favored for the detection of TCs due to its operational simplicity, cost-effectiveness, and rapid response [11, 12]. In particular, Eu^{3+}-based luminescent probes show great promise because of their large Stokes shift, long emission lifetime, and narrow emission bands [13–15]. The β-diketone structure of TCs allows them to coordinate with Eu^{3+} and sensitize its emission via the antenna effect, thereby significantly enhancing the characteristic Eu^{3+} luminescence and providing a basis for trace detection. Nevertheless, single-signal response probes are prone to interference from instrumental and environmental factors, limiting their reliability [16]. Ratiometric sensing overcomes this drawback by incorporating an internal reference for self-calibration, thereby improving accuracy and selectivity [17, 18]. Another advantage of ratiometric probes is their capacity to produce visible color changes, enabling straightforward naked-eye assessment [19]. Moreover, integration with smartphone technology has recently enabled the creation of effective portable platforms for on-site quantitative analysis [20–22].

Zinc gallogermanate, a solid solution formed by two well-studied oxides-$ZnGa_2O_4$ spinel and Zn_2GeO_4 willemite-has emerged as a novel oxide phosphor exhibiting properties superior to those of pure $ZnGa_2O_4$ or Zn_2GeO_4 [23]. For instance, Cr^{3+}-doped $Zn_3Ga_2Ge_2O_{10}$, which features ultralong super-long near-infrared persistent luminescence, has been successfully applied in bioimaging [24, 25]. In our previous work, various optical sensing platforms were constructed based on Cr^{3+}-doped zinc gallogermanate persistent luminescence nanomaterials [26], demonstrating that zinc gallogermanate is a promising luminescent nanomaterial with chemical stability, tunable luminescence, and ease of synthesis and functionalization. On the other hand, undoped zinc gallogermanate with blue luminescence is also a highly effective phosphor. It can serve as an ideal internal reference and a stable host matrix for Eu^{3+} modification-an application that, to the best of our knowledge, has not yet been reported.

In this work, we synthesized a Eu^{3+}-modified zinc gallogermanate nanomaterial (ZGGO-Eu^{3+}), which serves as a ratiometric luminescent probe for the rapid, sensitive, and visual detection of TC, as illustrated in Scheme 1. Unlike previously reported single-emission probes or physically mixed dual-emission sensing systems, the proposed ZGGO-Eu^{3+} nanoprobe integrates the intrinsic blue emission of ZGGO and the TC-responsive red emission of surface-coordinated Eu^{3+} within one nanoplatform. Upon the addition of TC, the Eu^{3+} emission at 618 nm was dramatically enhanced via the antenna effect, while the intrinsic luminescence of the ZGGO matrix at 465 nm was concurrently quenched due to the inner filter effect (IFE). These opposite emission

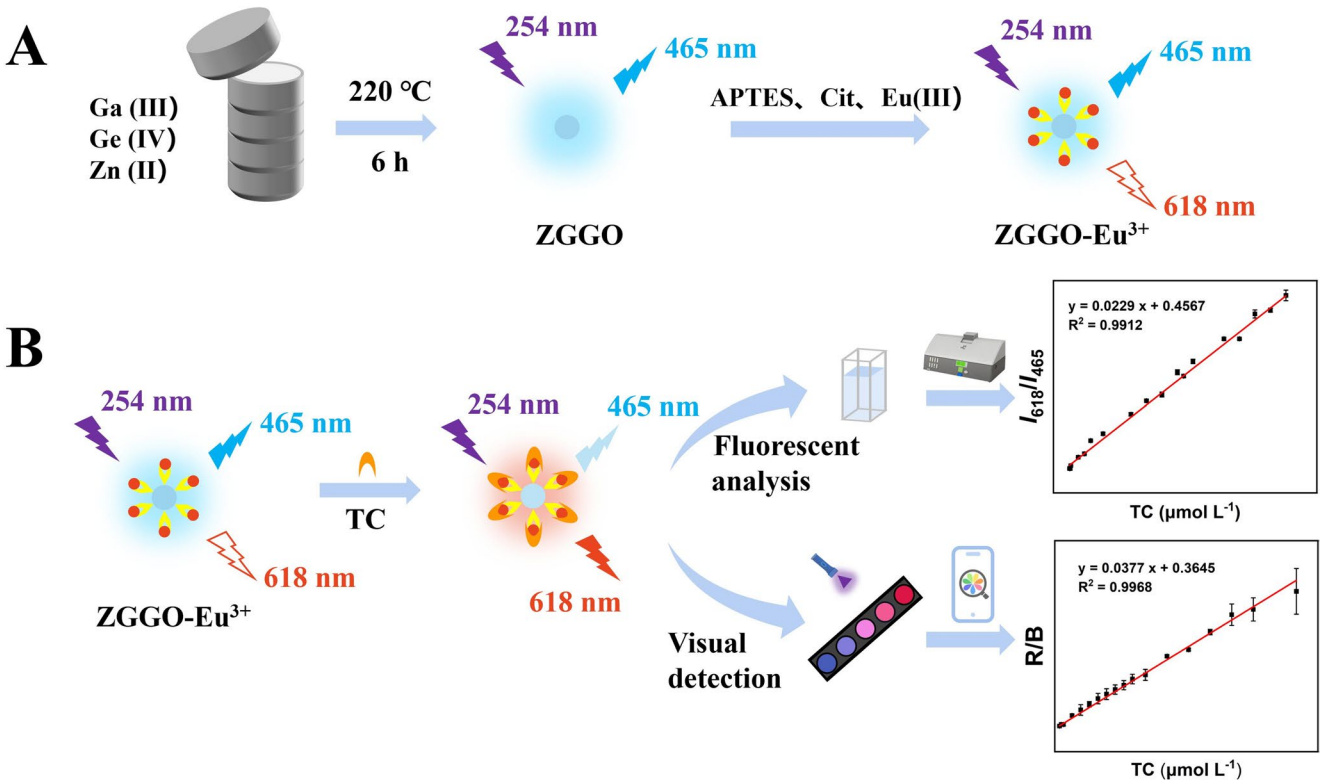

Scheme 1 Schematic illustration of ZGGO-Eu^{3+} synthesis and dual-platform detection for TC

changes generated a self-calibrated ratiometric signal, enabling reliable TC quantification based on the luminescence intensity ratio I_{618}/I_{465}. A linear relationship between I_{618}/I_{465} and TC concentration was established using a spectrofluorometer. Leveraging the distinct color transition from blue to red under UV irradiation, the ratiometric response was further coupled with smartphone-assisted RGB analysis to construct a low-cost and portable visual detection platform. This integrated probe design and readout strategy highlight the novelty and practical applicability of the proposed method for on-site screening of TC residues in food samples.

Experimental

Materials and instrumentation

This section has been presented in detail in the Supporting Information.

Synthesis of ZGGO and ZGGO-Eu^{3+}

This section has been presented in detail in the Supporting Information.

Fluorescence spectrophotometer-based detection of TC

To construct the calibration curve, 900 µL Tris-HCl buffer (50 mM, pH 8.5) containing the ZGGO-Eu^{3+} probe (1 mg mL^{-1}) was mixed with 100 µL TC standard solutions at different concentrations, giving final TC concentrations ranging from 0 to 90 µmol L^{-1}. After incubation for 10 min, fluorescence spectra were recorded over the range of 450–700 nm under excitation at 254 nm using an LP450 filter, and the fluorescence intensities at 465 and 618 nm were recorded. Each experiment was independently repeated three times, and the results were expressed as the mean values. The calibration curve was established by plotting the luminescence intensity ratio (I_{618}/I_{465}) against the TC concentration, thereby establishing a ratiometric fluorescence method for quantitative TC detection.

Smartphone-assisted visual detection of TC

A 180 µL aliquot of ZGGO-Eu^{3+} solution (1 mg mL^{-1}) was added to a black 96-well plate, followed by the addition of 20 µL TC standard solutions with different concentrations to obtain final TC concentrations ranging from 0 to 75 µmol L^{-1}. After incubation 10 min, the well plate was placed in the visual platform (Fig. S1), where the fixed distance between the well plate and the UV lamp was 10 cm. Luminescence images were then captured using a smartphone (iPhone 15) in the native camera mode with 2× optical zoom. The RGB values of the fluorescence images in each well were extracted using Adobe Photoshop 2021, and the red-to-blue channel ratio (R/B) was calculated. Each experiment was independently repeated three times, and the results were expressed as the mean values. The calibration curve was constructed by plotting the R/B value against the TC concentration, thereby establishing a visual quantitative detection method based on smartphone image analysis.

Selectivity and anti-interference experiments

In order to evaluate the selectivity and anti-interference ability of the ZGGO-Eu^{3+} fluorescent probe, common interfering substances found in biological samples were selected [27], including NaCl (Na^+), KCl (K^+), $CaCl_2$ (Ca^{2+}), $MgCl_2$ (Mg^{2+}), $FeCl_3$ (Fe^{3+}), $CuCl_2$ (Cu^{2+}), $Zn(NO_3)_2$ (Zn^{2+}), histamine (Hist), glutamate (Glu), cysteine (Cys), methionine (Met), arginine (Arg), serine (Ser), phenylalanine (Phe), oxytetracycline (OTC), doxycycline (DOX), enrofloxacin (ENR), norfloxacin (NOR), and ciprofloxacin (CIP). The concentration of the interfering substances was 200 µmol L^{-1} each and TC was 20 µmol L^{-1}. All other experimental conditions are described in the sections "Fluorescence spectrophotometer-based detection" and "Smartphone-assisted visual detection".

Analysis of TC in real samples

Live crucian carp (*Carassius auratus*), perch (*Lateolabrax japonicus*) and Wuchang bream (*Megalobrama amblycephala*) were purchased from a local wet market. Sample pretreatment is described in the Supporting Information. Aliquots (100 µL) of TC standard solutions at different concentrations were added to 900 µL of the pretreated fish sample extracts containing the ZGGO-Eu^{3+} probe (1 mg mL^{-1}). The subsequent fluorescence measurements were performed under the same conditions as those described in "Fluorescence spectrophotometer-based detection of TC". For smartphone-assisted visual detection, 180 µL of the pretreated fish sample extract containing ZGGO-Eu^{3+} probe (1 mg mL^{-1}) was first dispensed into each well of a 96-well plate, followed by the addition of 20 µL of TC standard solution at different concentrations. The imaging and RGB analysis procedures were performed under the

same conditions as those described in "Smartphone-assisted visual detection of TC".

Results and discussion

Synthesis and characterization of ZGGO-Eu^{3+} nanoprobe

White ZGGO (Fig S2) was synthesized via a solvothermal method. XRD pattern of the product (Fig S3) indicated that the obtained sample was a mixed phase composed of $ZnGa_2O_4$ and Zn_2GeO_4 [28]. TEM images (Fig. 1A) showed that the ZGGO particles were generally quasi-ellipsoidal, with a certain degree of size variation. Statistical analysis of 100 randomly selected nanoparticles revealed an average particle size of approximately 49.9 ± 20.4 nm (Fig S4). The HRTEM image (Fig. 1B) displayed clear lattice fringes with an interplanar spacing of approximately 0.29 nm, which could be indexed to the (220) plane of $ZnGa_2O_4$ with a cubic spinel structure.

The functionalization proceeded through sequential surface reactions. Anchoring of APTES produced amine-terminated ZGGO. These amine groups then underwent condensation with citric acid molecules, effectively tethering them on the surface. The carboxylic acid moieties of the grafted citric acid ultimately facilitated the coordination and stable immobilization of Eu^{3+}, forming the final ZGGO-Eu^{3+} probe. FTIR spectra (Fig. 1C) revealed the changes upon different modification. An absorption band at 3260 cm^{-1}, assigned to the N-H stretching vibration, and an asymmetric stretching vibration band of -CH_2- at 2938 cm^{-1} were observed after APTES treatment. Meanwhile, the O-Si-O stretching vibration bands at 1029 and 1126 cm^{-1} further confirmed the successful introduction of APTES onto the material surface [29]. The presence of absorption

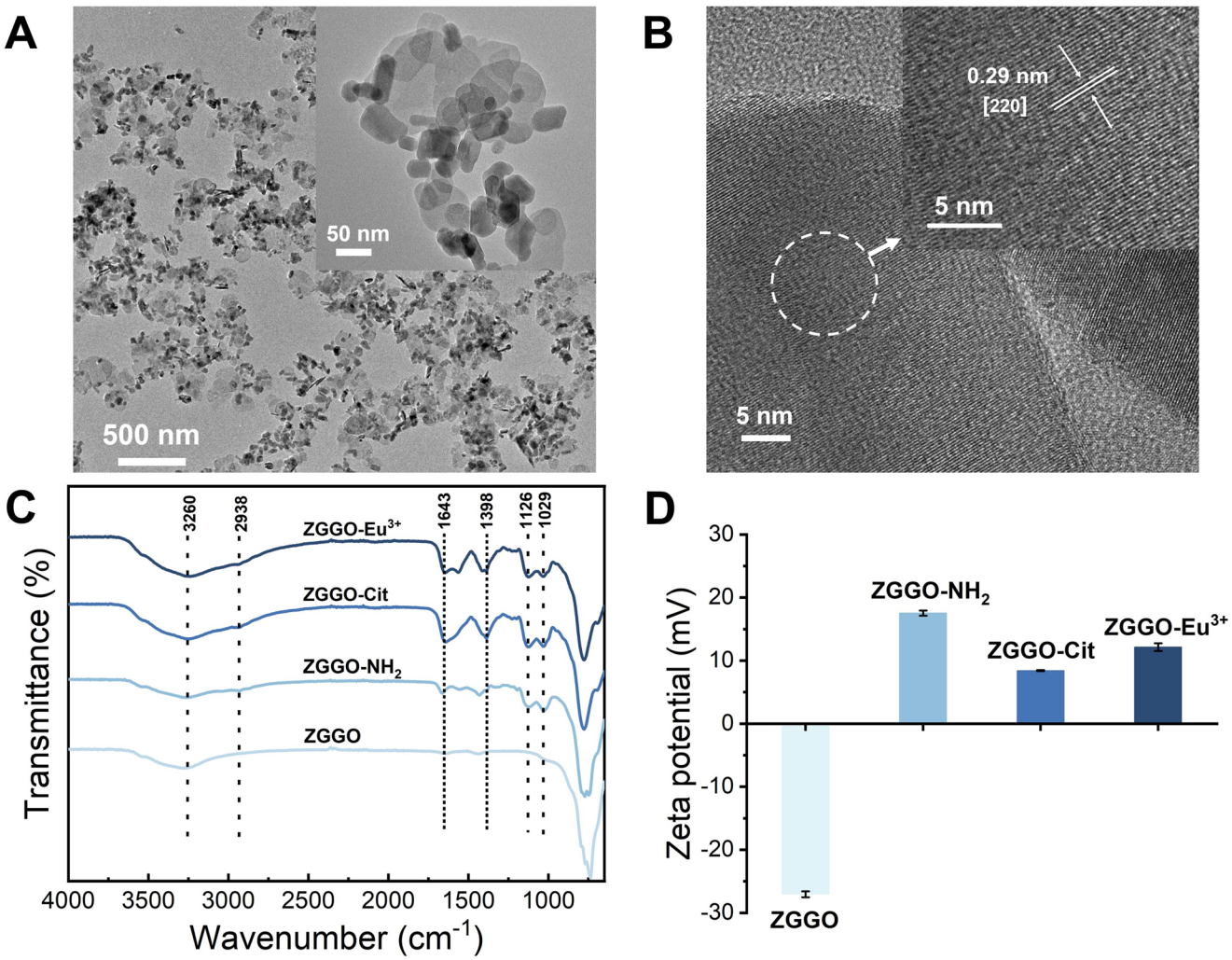

Fig. 1 (**A**) TEM image of ZGGO, the inset shows a magnified TEM image of ZGGO nanoparticles. (**B**) HRTEM image of ZGGO, the inset shows the lattice fringes. (**C**) FT-IR spectra of ZGGO, ZGGO-NH_2, ZGGO-Cit and ZGGO-Eu^{3+}. (**D**) Zeta potentials of ZGGO, ZGGO-NH_2, ZGGO-Cit and ZGGO-Eu^{3+}

peaks at 1643 cm^{-1} and 1398 cm^{-1}, which are attributed to the asymmetric and symmetric stretching vibrations of the -COO- group [30, 31], respectively, confirms the successful grafting of citric acid onto the nanomaterial surface. The subsequent attenuation of the peak at 1643 cm^{-1} in the final ZGGO-Eu^{3+} spectrum indicated the coordination of Eu^{3+} ions with carboxylate groups [32], thereby validating the successful assembly of the probe.

Zeta potential measurements (Fig. 1D) tracked the surface charge changes. The initial negative potential of ZGGO (-27.5 mV) was converted to a positive value (+17.5 mV) after APTES grafting, confirming successful amination. Subsequently, coupling with citric acid decreased the potential to +8.4 mV, due to the introduction of carboxyl groups. Finally, the chelation of Eu^{3+} ions increased the potential to +12.1 mV, attributed to the binding of the positively charged metal ions [33]. ICP-MS was used to compare the elemental compositions of ZGGO and ZGGO-Eu^{3+}. As shown in Table S1, Zn, Ga, and Ge were detected in both samples, whereas Eu was not detected in pristine ZGGO. In contrast, an obvious Eu signal was observed in ZGGO-Eu^{3+}, with a concentration of 16.87 ppb, confirming the successful introduction of Eu^{3+} into the ZGGO system.

Mechanism of TC response by using ZGGO-Eu^{3+}

To elucidate the ratiometric fluorescence response mechanism of the ZGGO-Eu^{3+} probe toward TC, spectral overlap, fluorescence lifetime, fluorescence response, and surface charge variation were systematically investigated. The results demonstrate that TC induced opposite changes in the dual-emission signals, namely the attenuation of the blue emission from the ZGGO matrix and the enhancement of the characteristic red emission of Eu^{3+}. The decrease in the blue emission was mainly attributed to the primary IFE. As shown in Fig. 2A, TC exhibits a broad absorption band in the range of 200–400 nm, which substantially overlapped with the excitation spectrum of ZGGO-Eu^{3+}. To quantitatively assess this overlap, the normalized excitation spectrum of ZGGO-Eu^{3+} and the UV absorption spectrum of TC were integrated, and the overlap ratio was calculated as follows:

$$\text{Overlap ratio } (\%) = \frac{\int_{\lambda_1}^{\lambda_2} S_{\text{overlap}(\lambda)\text{d?}}}{\int_{\lambda_1}^{\lambda_2} S_{\text{ex}(\lambda)\text{d?}}} \times 100\%$$

where $S_{ex}(\lambda)$ represents the normalized excitation spectrum of ZGGO-Eu^{3+}, and $S_{overlap}(\lambda)$ denotes the overlapping region between the TC absorption spectrum and the ZGGO-Eu^{3+} excitation spectrum. Within the range of 200–350 nm, the integrated area of the ZGGO-Eu^{3+} excitation spectrum was 43.82, while that of the overlapping region was 38.21, giving an overlap ratio of approximately 87.2%. This high overlap ratio provides direct quantitative evidence for the primary IFE. In contrast, TC showed only weak absorbance near the blue emission peak of ZGGO at 465 nm, indicating that reabsorption of the emitted light was limited and that the secondary IFE was not predominant. Moreover, the UV

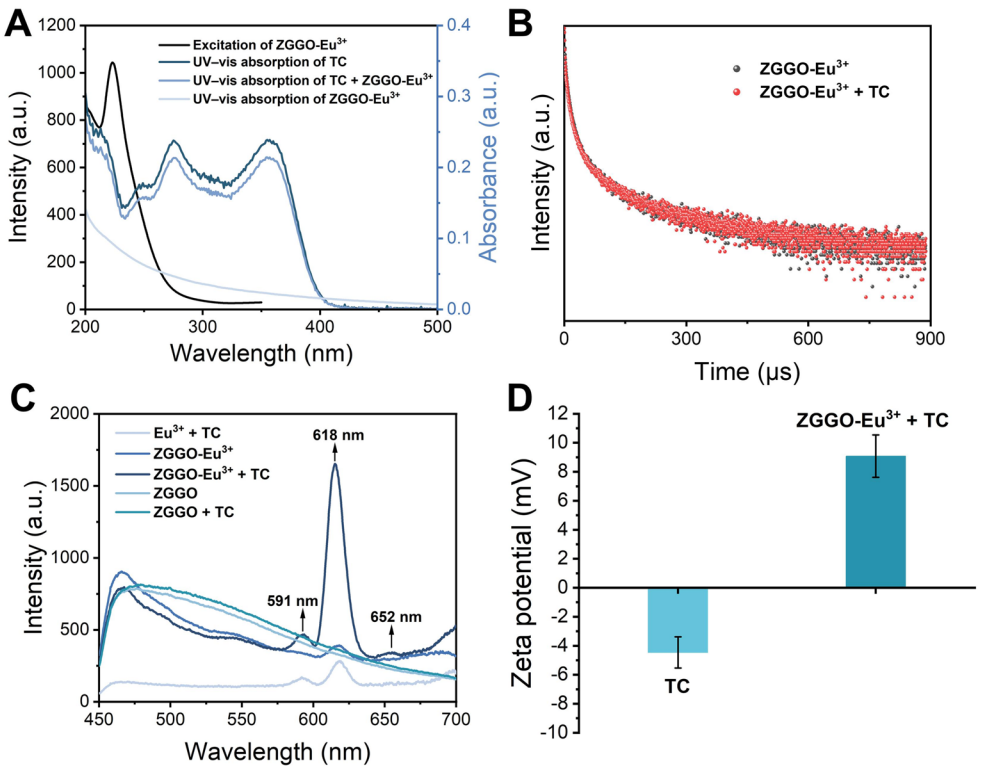

Fig. 2 (**A**) The excitation spectrum of ZGGO-$Eu^{3+}$and UV-vis absorption spectrum of different solutions (single TC, single ZGGO-Eu^{3+} and ZGGO-Eu^{3+} with TC) (the concentrations of ZGGO-Eu^{3+} and TC were 1 mg mL^{-1} and 0.1 mg mL^{-1}, respectively). (**B**) Fluorescence lifetime of ZGGO-Eu^{3+} (1 mg mL^{-1}) in the absence / presence of TC (10 μmol L^{-1}). (**C**) The emission spectra of different solutions (Eu^{3+}, ZGGO, ZGGO-Eu^{3+}, ZGGO with TC and ZGGO-Eu^{3+} with TC) under the excitation of 254 nm with a longpass filter 450 nm (the concentrations of Eu^{3+}, ZGGO, and ZGGO-Eu^{3+} were all 1 mg mL^{-1}, and the concentration of TC was 10 μmol L^{-1}). (**D**) Zeta potential of TC and ZGGO-Eu^{3+} with TC

absorption spectrum of the ZGGO-Eu^{3+}/TC system retained the main absorption features of TC without any distinct new absorption band, indicating that the IFE mainly originates from the intrinsic UV absorption of TC rather than from newly formed absorbing species. As shown in Fig. 2B, the fluorescence lifetimes of ZGGO-Eu^{3+} changed only slightly after interaction with TC, from 29.5 to 26.6 μs. Such a minor lifetime variation indicates that dynamic quenching is not the dominant pathway, further supporting an IFE-dominated attenuation process.

The TC-induced enhancement of the red emission at 618 nm is mainly related to Eu^{3+} sensitization rather than the ZGGO matrix itself. As shown in Fig. 2C, pristine ZGGO showed no obvious emission enhancement at 618 nm after interaction with TC, indicating that the ZGGO matrix alone cannot generate the red fluorescence response. Therefore, the introduction of Eu^{3+} luminescent centers is essential for constructing the 618 nm response signal. Although the Eu^{3+}/TC complex exhibited only weak luminescence, likely due to nonradiative energy dissipation caused by coordinated water molecules, the Eu^{3+} emission was markedly enhanced after Eu^{3+} was immobilized on citric acid-modified ZGGO. This enhancement indicates that the citric acid moiety on ZGGO surface provide a more rigid and favorable coordination microenvironment for Eu^{3+}, thereby effectively sensitizing its luminescence via the antenna effect. After interaction with TC, the ZGGO-Eu^{3+} probe exhibited a dual-emission profile, with the emission at 465 nm originating from the ZGGO matrix and the peaks at 591, 618, and 652 nm corresponded to the characteristic $^5D_0 \rightarrow {}^7F_{1-3}$ transitions of Eu^{3+} [34]. The interaction between TC and ZGGO-Eu^{3+} was further supported by zeta potential analysis. As shown in Fig. 2D, the zeta potentials of TC, ZGGO-Eu^{3+}, and the ZGGO-Eu^{3+}/TC system were −4.46, +12.13, and +9.07 mV, respectively. After TC addition, the surface potential decreased from +12.13 to +9.07 mV, indicating electrostatic interaction between negatively charged TC and the positively charged ZGGO-Eu^{3+} probe. This interaction promotes the enrichment of TC on the probe surface and facilitates its coordination with Eu^{3+} through oxygen-containing functional groups, providing the spatial proximity required for efficient TC-to-Eu^{3+} energy transfer and enhanced red emission.

In summary, the response mechanism of the ZGGO-Eu^{3+} probe toward TC mainly involves two processes. On the one hand, TC weakens the effective excitation of the ZGGO matrix through a primary IFE, thereby decreasing its blue emission. On the other hand, TC can be enriched on the probe surface via electrostatic adsorption and coordinate with Eu^{3+} through the oxygen-containing functional groups in its molecular structure, consequently sensitizing the characteristic red emission of Eu^{3+}. These dual effects result in a ratiometric response of the ZGGO-Eu^{3+}/TC system, characterized by decreased blue emission and enhanced red emission, providing a mechanistic basis for the ratiometric fluorescence detection of TC.

Optimization and optical properties of ZGGO-Eu^{3+}

The ZGGO-Eu^{3+} nanomaterial was employed as a dual-emission ratiometric probe for TC sensing. To achieve optimal analytical performance, the reference emission wavelength, buffer pH, and incubation time were optimized. The emission maximum of the probe was found to shift with changes in instrumental voltage and probe concentration (Fig S5A, S5B), whereas the emission at 465 nm remained relatively stable and was therefore selected as the reference signal. Accordingly, the I_{618}/I_{465} ratio was used for all subsequent quantitative analyses. The effect of buffer pH was investigated, and the maximum I_{618}/I_{465} ratio was observed at pH 8.5 (Fig. 3A). Finally, the reaction kinetics showed that the I_{618}/I_{465} ratio increased with incubation time and reached a plateau at 10 min (Fig. 3B), indicating that the interaction between the probe and TC had reached equilibrium. Thus, pH 8.5 and incubation time of 10 min were selected as the optimal conditions for further experiments.

Stability analysis of the ZGGO-Eu^{3+} probe

To evaluate the stability of the ZGGO-Eu^{3+} probe, different testing conditions were investigated, including inter-day (Fig S6A), batch-to-batch (Fig S6B), intra-day (Fig S6C), and various temperatures (Fig S6D). The I_{618}/I_{465} ratio remained relatively stable during storage over five consecutive days, continuous testing within 10 h, and analysis of five independently prepared batches, with only small deviations observed. These results indicate that the probe exhibits good storage stability, intra-day stability, and batch-to-batch reproducibility. In addition, the ratiometric fluorescence signal showed only slight increase over the temperature range from 4 to 45 °C, suggesting good tolerance to temperature changes. Overall, these results demonstrate that the ZGGO-Eu^{3+} probe possesses satisfactory stability and is suitable for reliable analytical detection.

Performance of the ZGGO-Eu^{3+} nanoprobe for TC detection

The sensing performance of the ZGGO-Eu^{3+} probe was first evaluated with a fluorescence spectrophotometer. As shown in Fig. 4A, under 254 nm excitation, the emission intensity at 618 nm gradually increased with increasing TC concentration, while the emission intensity at 465 nm decreased simultaneously, confirming the dual-signal ratiometric

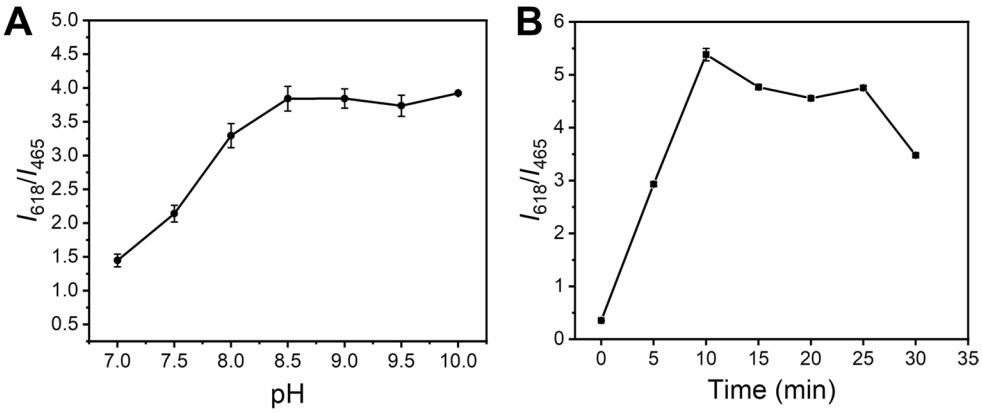

Fig. 3 (**A**) Effect of pH on the I_{618}/I_{465} of ZGGO-Eu^{3+} with TC. (**B**) Effect of response time on the I_{618}/I_{465} of ZGGO-Eu^{3+} with TC. (The concentrations of ZGGO-Eu^{3+} and TC were 1 mg mL^{-1} and 10 μmol L^{-1}, respectively)

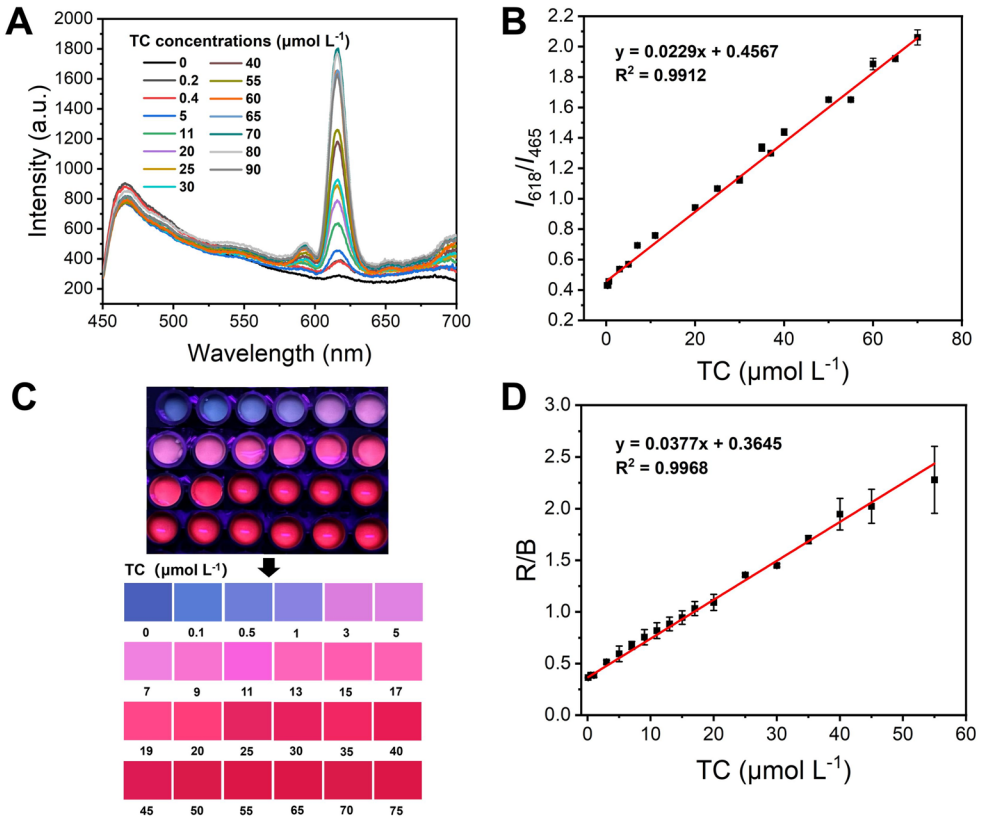

Fig. 4 (**A**) Fluorescence spectra of ZGGO-Eu^{3+} containing TC concentrations of 0–90 μmol L^{-1}. (**B**) The linear curve fitting relationship between I_{618}/I_{465} and TC. (**C**) Fluorescence color images of ZGGO-Eu^{3+} containing TC concentrations of 0–75 μmol L^{-1} under 254 nm UV excitation. (**D**) The linear curve fitting relationship between R/B and TC

response of the probe. At TC concentrations above 70 μmol L^{-1}, the 618 nm emission began to decline, probably because excessive TC absorbed a large fraction of the excitation light, thereby limiting the effective excitation and sensitization of Eu^{3+}. Therefore, the linear range was 0.2–70 μmol L^{-1}. Within this range, the fluorescence intensity ratio I_{618}/I_{465} showed good linearity toward TC concentration (Fig. 4B), following the equation $y=0.0229x+0.4567$ and $R^2=0.9912$. The precision of the developed ratiometric fluorescence method for eleven replicate detections of 10 μmol L^{-1} TC was 1.7% relative standard deviation (RSD) (Table S2). The limit of detection (LOD) and limit of quantification (LOQ) were calculated as follows:

$$\mathrm{LOD} = \frac{3\sigma}{k}$$
$$\mathrm{LOQ} = \frac{10\sigma}{k}$$

where σ is the standard deviation of the blank signal obtained from 12 independent blank measurements ($n=12$), and k is the slope of the calibration curve. The LOD and LOQ were calculated to be 169.5 nmol L^{-1} and 565.0 nmol L^{-1}, respectively. The obtained LOD is lower than the maximum residue limits set by the EU and China (0.225 μmol L^{-1}), and is also lower than many previously reported fluorescence methods for TC detection (Table S3).

For visual and on-site application, the fluorescence color response of the nanoprobe was further investigated.

Under 254 nm UV irradiation, the probe solution showed a TC concentration-dependent fluorescence color evolution, arising from the enhanced red Eu^{3+} emission and weakened blue ZGGO emission. This visible change enabled semi-quantitative naked-eye screening of TC. However, when the TC concentration exceeded 55 μmol L^{-1}, the red fluorescence response tended to reach saturation, and no obvious further color change was observed (Fig. 4C). To achieve quantitative analysis, a smartphone-assisted platform based on RGB analysis was constructed. A good linear relationship between the R/B value and TC concentration was obtained over the range of 0.1–55 μmol L^{-1} (Fig. 4D), following the equation $y = 0.0377x + 0.3645$ with $R^2 = 0.9968$. The precision of the smartphone-assisted visual method for eleven replicate detections of 10 μmol L^{-1} TC was 3.1% relative standard deviation (RSD) (Table S2). Similarly, each concentration was measured in triplicate ($n = 3$), and the LOD and LOQ were calculated using the standard deviation of 12 blank measurements ($n = 12$). The smartphone-based method provided an LOD of 85.9 nmol L^{-1} and an LOQ of 286.3 nmol L^{-1}. As summarized in Table S4, this portable platform provides competitive analytical performance for on-site visual quantification of TC, especially in terms of sensitivity and operational convenience.

Selectivity and anti-interference ability of ZGGO-Eu^{3+} for TC detection

The specificity of the ZGGO-Eu^{3+} nanoprobe was evaluated by examining its fluorescence intensity to various potential interferents. As illustrated in Fig. 5A, a pronounced increase in the I_{618}/I_{465} ratio was observed only for tetracycline-class antibiotics, including TC, OTC and DOX, whereas non-tetracycline antibiotics, including NOR, ENR and CIP, induced only negligible signal changes. These results demonstrate that the ZGGO-Eu^{3+} nanoprobe exhibits good specificity toward TCs. The anti-interference capability of the nanoprobe was further assessed in the presence of common coexisting substances, such as metal ions (Na^+, K^+, Ca^{2+}, Mg^{2+}, Cu^{2+}, Fe^{3+}, Zn^{2+}), amino acids (Glu, Cys, Met, Phe, Ser, Arg) and Hist. As shown in Fig. 5B, the TC-induced fluorescence response was well maintained in the presence of most interferents, demonstrating good anti-interference capability. The slight signal decrease observed in the presence of Cu^{2+} and Fe^{3+} may be related to their possible complexation or oxidative interaction with TC, which could partially affect TC-mediated Eu^{3+} sensitization.

The visual and RGB responses of the smartphone-assisted platform were also assessed. As shown in Fig. 5C, tetracycline-class antibiotics, particularly TC and DOX,

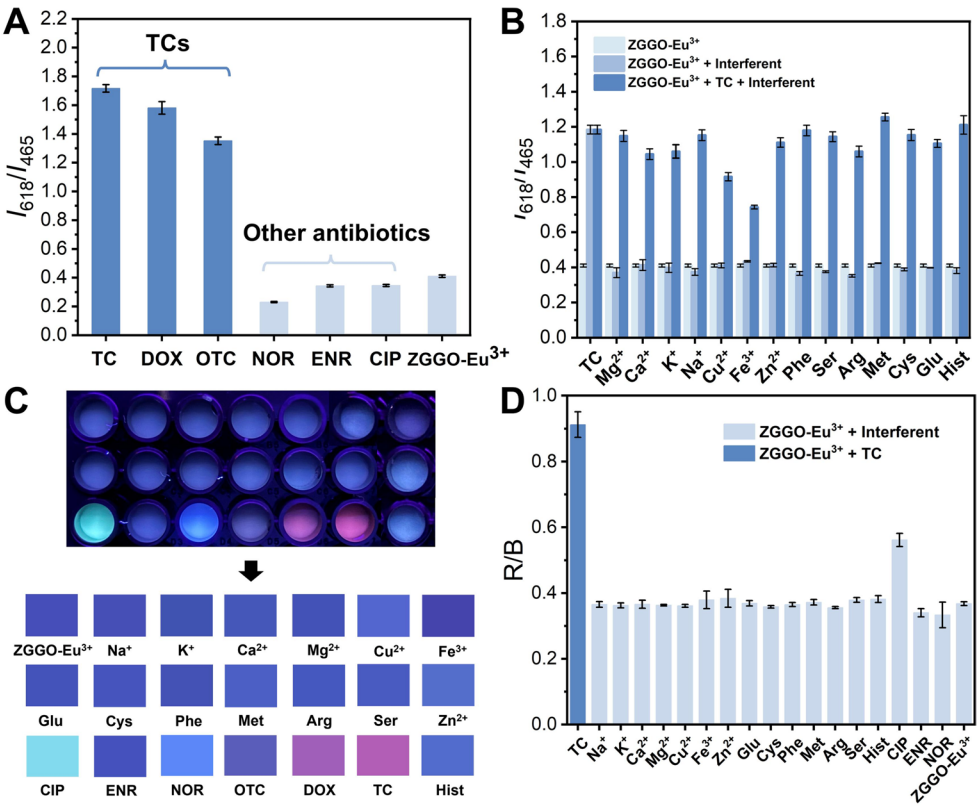

Fig. 5 (**A**) Fluorescent responses of ZGGO-Eu^{3+} to TC and other antibiotics (concentration of each antibiotic was 10 μmol L^{-1}). (**B**) Fluorescent responses of ZGGO-Eu^{3+} to other interferential substances in the absence and presence of TC (10 μmol L^{-1}). (**C**) Fluorescence color images of ZGGO-Eu^{3+} in the presence of 10 μmol L^{-1} interfering substance concentrations under 254 nm UV excitation. (**D**) R/B responses of ZGGO-Eu^{3+} to TC and other interferential substances (10 μmol L^{-1})

produced an obvious red fluorescence response that was readily distinguishable from the blank by the naked eye. In contrast, CIP and NOR showed different fluorescence colors, while ENR and most common ions, amino acids, and histamine caused no apparent color change. Consistently, TC produced the highest R/B value, whereas most interferents gave much lower values close to the blank level (Fig. 5D). Although CIP caused a slight increase in the R/B value, its response remained clearly lower than that of TC. These results demonstrate that the smartphone-assisted visual platform provides good visual discrimination and anti-interference performance for rapid TC screening.

Validation and application to real samples

TCs were detected in all three commonly consumed fish species including perch, crucian carp, and Wuchang bream, using the developed fluorescence and smartphone-assisted visualization methods (Table 1). To validate the reliability of the proposed methods, the same samples were also analyzed by HPLC as a reference method. Representative HPLC chromatograms showed well-defined TC peaks in the fish samples, with retention behavior consistent with that of the TC standard and no obvious matrix interference (Fig S7, Fig S8). As summarized in Table 1, the TC concentrations determined by the proposed fluorescence and visualization methods were in highly consistent with those obtained by HPLC. Paired *t*-tests further confirmed this agreement, as the *p* values for both the fluorescence method versus HPLC and the visualization method versus HPLC were greater than 0.05 (Table S5), indicating no statistically significant difference between the proposed methods and HPLC. In addition, spike-and-recovery experiments were performed at three concentration levels of 5, 20, and 50 μmol L^{-1}. The recoveries ranged from 93.3% to 117.4% for the fluorescence method and from 86.1% to 117.8% for the visualization method (Table 2), demonstrating acceptable accuracy in real-sample analysis. These results confirm that the proposed fluorescence and smartphone-assisted visualization methods are reliable and practically applicable for TCs determination in fish samples. (The detailed data for the real samples are presented in Table S6 and Table S7)

Table 1 TCs detection results with the proposed fluorescence and visualization methods were validated by HPLC

Samples	TCs concentration found (μmol L^{-1}, Mean ± SD, $n = 3$)		
	Fluorescence method	Visualization method	HPLC
Crucian carp-1	2.33 ± 0.18	2.39 ± 0.31	2.25 ± 0.12
Crucian carp-2	1.42 ± 1.28	1.49 ± 0.25	1.40 ± 0.02
Perch-1	1.89 ± 0.15	1.96 ± 0.19	1.82 ± 0.08
Perch-2	1.56 ± 0.25	1.60 ± 0.31	1.56 ± 0.09
Wuchang bream-1	1.49 ± 0.08	1.50 ± 0.34	1.44 ± 0.01
Wuchang bream-2	1.61 ± 0.61	1.69 ± 0.08	1.68 ± 0.04

Conclusion

A ZGGO-Eu^{3+}-based dual-readout ratiometric nanoprobe was proposed for the sensitive, convenient, and on-site-oriented detection of TCs in food samples. The nanoprobe was constructed through sequential surface functionalization of ZGGO, which provided stable coordination sites for Eu^{3+} immobilization. Upon interaction with TC, the antenna effect between TC and Eu^{3+} enhanced the emission at 618 nm of Eu^{3+}, while the primary inner filter effect attenuated the ZGGO matrix emission at 465 nm, enabling ratiometric fluorescence detection based on two oppositely varying signals. By integrating the fluorescence response with smartphone-based RGB analysis, a portable visual sensing platform was established for rapid TCs screening without reliance on large laboratory instruments. The proposed methods exhibited a wide linear range, low detection limit, and satisfactory analytical accuracy in real-sample analysis. When applied to three commonly consumed fish species, the results were consistent with those obtained by HPLC, and the recoveries for spiked samples ranged from 86.1% to 117.8%, well within the acceptable range. Owing to its simple operation, short response time, and low equipment requirement, this strategy shows promise for cost-effective field screening and future development into portable detection kits for animal-derived food safety monitoring. Nevertheless, standardized sample pretreatment,

Table 2 Spike recoveries of TC in fish samples by fluorescence and visualization methods

Samples	Recovery (%, Mean ± SD, $n = 3$)					
	Fluorescence method			Visualization method		
	5 μmol L^{-1}	20 μmol L^{-1}	50 μmol L^{-1}	5 μmol L^{-1}	20 μmol L^{-1}	50 μmol L^{-1}
Crucian carp-1	103.6 ± 8.1	99.1 ± 1.6	100.7 ± 5.0	117.8 ± 1.9	94.5 ± 1.7	86.1 ± 4.6
Crucian carp-2	106.5 ± 2.1	103.4 ± 5.5	93.3 ± 6.3	117.6 ± 1.3	91.8 ± 1.5	107.7 ± 9.1
Perch-1	106.8 ± 5.4	103.6 ± 1.5	117.4 ± 2.9	94.5 ± 4.3	98.3 ± 2.9	96.6 ± 6.6
Perch-2	104.4 ± 6.3	105.9 ± 3.6	111.6 ± 2.8	106.9 ± 1.7	102.6 ± 1.7	96.6 ± 5.6
Wuchang bream-1	99.8 ± 2.9	98.7 ± 0.3	97.1 ± 3.3	112.3 ± 8.4	95.9 ± 4.2	98.9 ± 2.0
Wuchang bream-2	106.6 ± 9.2	94.1 ± 4.7	105.3 ± 3.7	113.4 ± 6.3	111.8 ± 2.2	106.5 ± 3.6

controlled imaging conditions, integrated device design, and validation with more diverse real samples should be further addressed before routine application. Overall, this work provides a reliable and practical ratiometric sensing strategy for TCs monitoring in animal-derived foods.

Supplementary Information The online version contains supplementary material available at https://doi.org/10.1007/s00604-026-08107-2.

Acknowledgements This work was supported by the National Natural Science Foundation of China 42421005, 22304063) and the Natural Science Foundation of Jiangsu Province, China (No. BK20231033).

Author contributions Xue-Yang Huang : Investigation, Methodology, Data curation, Writing – original draft. Li-Xia Yan : Methodology, Funding acquisition. Xu Zhao : Investigation, Methodology. Hua Lin : Investigation, Methodology. Li-Jian Chen : Conceptualization, Supervision, Writing – review & editing. Xiu-Ping Yan : Investigation, Methodology.

Data availability The data supporting the findings of this article have been included as part of the Supplementary Material.

Declarations

Competing interests The authors declare no competing interests.

References

1. Cui Y, Li Q, Qian J et al (2025) Simultaneous detection and removal of tetracycline antibiotics in water using silver-based metal-organic frameworks. Microchim Acta 192:140. https://doi.org/10.1007/s00604-025-07000-8
2. Li S, Li H, Li Y et al (2025) Selective ratiometric fluorescent detection of chlortetracycline in environmental water based on hydrolysis-induced emission. Microchim Acta 192:512. https://doi.org/10.1007/s00604-025-07394-5
3. Zhou R, Guo W, Wang J et al (2024) N-doped silicon QDs: Facile synthesis and application as sensor for discrimination and selective detection of oxytetracycline, tetracycline, and chlortetracycline in foods. Microchim Acta 191:698. https://doi.org/10.1007/s00604-024-06786-3
4. Li X, Fan K, Yang R et al (2020) A long lifetime ratiometrically luminescent tetracycline nanoprobe based on Ir(III) complex-doped and Eu^{3+}-functionalized silicon nanoparticles. J Hazard Mater 386:121929. https://doi.org/10.1016/j.jhazmat.2019.121929
5. Ameen SSM, Algethami FK, Omer KM (2026) Triple-emission output for improved color tonality discrimination via a dual-emissive Zn(II)/Eu(III) bi-ligand MOF probe toward ultrasensitive detection of tetracycline in diverse matrices. Microchem J 223:117326. https://doi.org/10.1016/j.microc.2026.117326
6. Zhang X, Li Z, Cui W et al (2024) Hydrothermal synthesis of a novel one-dimensional cadmium-based coordination polymer for effective detection of hazardous chemicals. J Inorg Organomet Polym Mater 34:4063–4071. https://doi.org/10.1007/s10904-024-03066-8
7. Shalaby AR, Salama NA, Abou-Raya SH et al (2011) Validation of HPLC method for determination of tetracycline residues in chicken meat and liver. Food Chem 124:1660–1666. https://doi.org/10.1016/j.foodchem.2010.07.048
8. Tsuji Kiyoshi, Robertson JH (1973) Formation of trimethylsilyl derivatives of tetracyclines for separation and quantitation by gas-liquid chromatography. Anal Chem 45:2136–2140. https://doi.org/10.1021/ac60334a037
9. Belhadj N, Lailliau M, Benoit R et al (2021) Experimental and kinetic modeling study of n-hexane oxidation. Detection of complex low-temperature products using high-resolution mass spectrometry. Combust Flame 233:111581. https://doi.org/10.1016/j.combustflame.2021.111581
10. Zhang T, Zhang X, Yu J et al (2024) Rapid determination of tetracyclines in drinking and environmental waters using fully automatic solid-phase extraction with ultra-performance liquid chromatography–tandem mass spectrometry. Molecules 29:2921. https://doi.org/10.3390/molecules29122921
11. Pu Q, Wang C, Yin X et al (2024) A ratiometric fluorescent dark box and smartphone integrated portable sensing platform based on hydrogen bonding induction for on-site determination of enrofloxacin. Food Chem 455:139876. https://doi.org/10.1016/j.foodchem.2024.139876
12. SSh MA, Omer KM (2024) Dual-state red-emitting zinc-based MOF accompanied by dual-mode and dual-state detection: Color tonality visual mode for the detection of tetracycline. ACS Appl Mater Interfaces 16:51376–51383. https://doi.org/10.1021/acsami.4c13115
13. Yue F, Zhao X, Chen X et al (2024) A dual-channel sensing platform for the cross-interference-free detection of tetracycline and copper ion. Talanta 279:126617. https://doi.org/10.1016/j.talanta.2024.126617
14. Zhang T, Zhang Z, Yao H et al (2025) Fluorescent smartphone sensing platform based on Eu^{3+}-functionalized metal-organic framework for ultra-sensitive detection of ciprofloxacin. Environ Res 285:122326. https://doi.org/10.1016/j.envres.2025.122326
15. Ameen SSM, Algethami FK, Omer KM (2026) Residual ofloxacin detection in food via paper-based and solution platforms using a dual-emissive MOF with wide-range triple-color emission. Food Chem 500:147452. https://doi.org/10.1016/j.foodchem.2025.147452
16. Guo L, Chen S, Yu Y-L et al (2021) A smartphone optical device for point-of-care testing of glucose and cholesterol using ag NPs/UiO-66-NH_2 -based ratiometric fluorescent probe. Anal Chem 93:16240–16247. https://doi.org/10.1021/acs.analchem.1c04126
17. Chen L, Li Z, Dou Y et al (2024) Ratiometric fluoroprobe based on Eu-MOF@Tb^{3+} for detecting tetracycline hydrochloride in freshwater fish and its application in rapid visual detection. J Hazard Mater 469:134045. https://doi.org/10.1016/j.jhazmat.2024.134045
18. SSh MA, Omer KM (2024) Merging dual antenna effect with target-insensitive behavior in bimetal biligand MOFs to form efficient internal reference signal: Color tonality-ratiometric designs. ACS Mater Lett 6:2339–2349. https://doi.org/10.1021/acsmaterialslett.4c00845
19. Fatah SA, Ameen SSM, Hassan PB et al (2026) Aptamer-gated luminescence enhancement and red-shift in a MOF: A ratiometric and color-tonality visual biosensor for pathogenic E. coli detection. Microchim Acta 193:154. https://doi.org/10.1007/s00604-025-07815-5
20. Liu W, Huang Y, Ji C et al (2024) Eu^{3+}-doped anionic zinc-based organic framework ratio fluorescence sensing platform: supersensitive visual identification of prescription drugs. ACS Sens 9:759–769. https://doi.org/10.1021/acssensors.3c02069
21. Qader IB, Ameen SSM, Qader HA et al (2025) Visual-based platform using sustainable intrinsic fluorescent Zn-based metal–organic framework for detection of folic acid in pharmaceutical formulations. J Inorg Organomet Polym Mater 35:888–897. https://doi.org/10.1007/s10904-024-03322-x
22. Yu L, Li X, Lu Y et al (2023) Simulation monitoring of tetracyclines in wastewater based on fluorescence image processing and

machine learning classifier. Sens Actuat B: Chem 385:133678. https://doi.org/10.1016/j.snb.2023.133678
23. Ren J, Xu X, Zeng H et al (2014) Novel self-activated zinc gallogermanate phosphor: The origin of its photoluminescence. J Am Ceram Soc 97:3197–3201. https://doi.org/10.1111/jace.13103
24. Pan Z, Lu Y-Y, Liu F (2012) Sunlight-activated long-persistent luminescence in the near-infrared from Cr^{3+}-doped zinc gallogermanates. Nat Mater 11:58–63. https://doi.org/10.1038/nmat3173
25. Abdukayum A, Chen J-T, Zhao Q et al (2013) Functional near infrared-emitting Cr^{3+} /Pr^{3+} co-doped zinc gallogermanate persistent luminescent nanoparticles with superlong afterglow for *in vivo* targeted bioimaging. J Am Chem Soc 135:14125–14133. https://doi.org/10.1021/ja404243v
26. Zhao X, Chen L-J, Zhao K-C et al (2019) Autofluorescence-free chemo/biosensing in complex matrixes based on persistent luminescence nanoparticles. Trends Anal Chem 118:65–72. https://doi.org/10.1016/j.trac.2019.05.025
27. Li C, Zeng C, Chen Z et al (2020) Luminescent lanthanide metal-organic framework test strip for immediate detection of tetracycline antibiotics in water. J Hazard Mater 384:121498. https://doi.org/10.1016/j.jhazmat.2019.121498
28. Zhang X, Hou X, Gao J et al (2023) Colour evolution of dynamic persistent luminescence of $Zn_3Ga_2Ge_2O_{10}$:Cr^{3+},Mn^{2+} phosphors for advanced anti-counterfeiting. J Mater Chem C 11:16631. https://doi.org/10.1039/D3TC03298A
29. Li X, Ma H, Deng M et al (2017) Europium functionalized ratiometric fluorescent transducer silicon nanoparticles based on FRET for the highly sensitive detection of tetracycline. J Mater Chem C 5:2149–2152. https://doi.org/10.1039/C7TC00305F
30. Chen J, Zhang Q, Xu F et al (2021) Bimetallic organic frame nanosheet fluorescent probe used for detecting tetracycline and folic acid. Microchem J 170:106673. https://doi.org/10.1016/j.microc.2021.106673
31. Han S, Yang L, Wen Z et al (2020) A dual-response ratiometric fluorescent sensor by europium-doped CdTe quantum dots for visual and colorimetric detection of tetracycline. J Hazard Mater 398:122894. https://doi.org/10.1016/j.jhazmat.2020.122894
32. Zhang L, Wang Y, Jia L et al (2021) Ultrasensitive and visual detection of tetracycline based on dual-recognition units constructed multicolor fluorescent nano-probe. J Hazard Mater 409:124935. https://doi.org/10.1016/j.jhazmat.2020.124935
33. Shen Y, Wei Y, Chen H et al (2022) Liposome-encapsulated aggregation-induced emission fluorogen assisted with portable smartphone for dynamically on-site imaging of residual tetracycline. Sens Actuat B: Chem 350:130871. https://doi.org/10.1016/j.snb.2021.130871
34. Xu J, Jia L, Ma Y et al (2012) Novel lanthanide hybrid functional materials for high performance luminescence application: The relationship between structures and photophysical behaviors. Mater Chem Phys 136:112–119. https://doi.org/10.1016/j.matchemphys.2012.06.038